Special Double Issue Article

B. Geppert*, D. Groeneveld, V. Loboda, A. Korotkov and A. Feldhoff

Finite-Element Simulations of a Thermoelectric Generator and Their Experimental Validation

Abstract: A versatile finite-element simulation tool was developed to predict the electric power output, the distributions of the electric and entropy potentials (i.e., the absolute temperature) and the local flux densities of electric charge and thermal energy (i.e., heat) for a thermoelectric generator. The input parameters are the thermogenerator architecture (i.e., geometries of different components and number of legs) and material properties such as specific electric conductivity, Seebeck coefficient and thermal conductivity. The finite-element simulation tool was validated by modeling a commercially available thermoelectric generator, which was based on semiconducting n- and p-type $Bi_{2-x}Sb_xTe_3$ with ceramic cover plates, and comparing the modeled voltage–current characteristics and power characteristics with experimental values for different temperature conditions. The geometric parameters could easily be determined from photomicrography and cross-sectional scanning electron microscopy observations. The electric conductivity and Seebeck coefficient were measured, as functions of temperature, from the integer module as leg-averaged values. The thermal conductivity was taken from literature data, which required estimating the compositions of components using energy-dispersive X-ray spectroscopy in the scanning electron microscope and their crystal structures using X-ray diffraction. Good agreement was found between the simulated and measured voltage–current and power–current characteristics. The finite-element simulation tool is versatile because it uses a script-based approach, which allows easy parameter changes and allows it to be adapted to thermogenerators consisting of different geometries and materials, including novel materials.

Keywords: thermoelectric generator, thermal energy, electric energy, energy conversion, finite-element method

DOI 10.1515/ehs-2015-0001

***Corresponding author: B. Geppert,** Institute of Physical Chemistry and Electrochemistry, Leibniz Universität Hannover, Hannover, Lower Saxony, Germany, E-mail: benjamin-geppert@pci.uni-hannover.de

D. Groeneveld, Institute of Physical Chemistry and Electrochemistry, Leibniz Universität Hannover, Hannover, Lower Saxony, Germany, E-mail: dennis_groeneveld@ewetel.net

V. Loboda: E-mail: vera_loboda@mail.ru, **A. Korotkov:** E-mail: korotkov@rphf.spbstu.ru, Integrated Electronics Department, St. Petersburg Polytechnic University, St. Petersburg, Russia

A. Feldhoff, Institute of Physical Chemistry and Electrochemistry, Leibniz Universität Hannover, Hannover, Lower Saxony, Germany, E-mail: armin.feldhoff@pci.uni-hannover.de

Introduction

The development and application of thermoelectric materials, for example, for harvesting electrical power from waste heat sources, is a current field of study that requires interdisciplinary investigations. The implementation of newly developed thermoelectric materials into thermoelectric generators (TEGs) benefits from modeling the thermoelectric properties of the generators with respect to the individual properties of the employed materials. A TEG is a device that transfers energy from thermal (entropy) current to electric current; see Fuchs (2010, 2014), Feldhoff (2015). Following the concept of energy carriers as outlined by Falk, Herrmann, and Schmid (1983), it is quite intuitive to use the term *thermal energy* E, th when energy flows together with entropy S and to use the term *electric energy* E, el when energy flows together with electric charge q. The most straightforward description of a thermoelectric device relies on considering the flux densities of the aforementioned fluid-like quantities because it links them by the respective potentials, which are the absolute temperature T for entropy and the electric potential φ for electric charge. The energy flux densities are then as follows; see Fuchs (2014), Feldhoff and Geppert (2014b, 2014a), Feldhoff (2015):

$$\vec{j}_{E,th} = T \cdot \vec{j}_S \quad [1]$$

$$\vec{j}_{E,el} = \varphi \cdot \vec{j}_q \quad [2]$$

The flux densities of entropy $\vec{j}_S$ and electric charge $\vec{j}_q$ in a thermoelectric material, that is subjected to gradients of thermal potential $\vec{\nabla}T$ and electric potential $\vec{\nabla}\varphi$, can be easily obtained if a thermoelectric material tensor is considered; see Feldhoff (2015):

$$\begin{pmatrix} \vec{j}_S \\ \vec{j}_q \end{pmatrix} = -\begin{pmatrix} \sigma \cdot \alpha^2 + \Lambda & \sigma \cdot \alpha \\ \sigma \cdot \alpha & \sigma \end{pmatrix} \cdot \begin{pmatrix} \vec{\nabla} T \\ \vec{\nabla} \varphi \end{pmatrix} \quad [3]$$

The thermoelectric tensor consists of three tensorial quantities; however, these quantities are treated as scalars. These are the specific electric conductivity σ under isothermal conditions (i.e., $\vec{\nabla} T = 0$, vanishing thermal potential gradient), the specific entropy conductivity Λ under electric open-circuited conditions (i.e., $\vec{j}_{q=0}$, vanishing electric current), and the so-called Seebeck coefficient α, which is defined as *entropy flow per flow of unit charge*; see Fuchs (2014), Feldhoff and Geppert (2014b, 2014a), Feldhoff (2015).

In principle, electric charge is bound to some particle with chemical potential μ, and in the concept of combined potentials, see Fuchs (2014), the electrochemical potential $\tilde{\mu} = \mu + q \cdot \varphi$ is the more accurate quantity. However, because gradients are relevant, when the chemical potential μ has a weak temperature dependence, the electric potential φ can be used as a good approximation rather than the electrochemical potential $\tilde{\mu}$ as in eqs [2] and [3]; see Feldhoff (2015).

To construct the basic unit of a thermoelectric generator, two materials with different algebraic signs for the Seebeck coefficient α (*entropy flow per flow of unit charge*) must be thermally connected in parallel and electrically connected in series. For $\alpha > 0$, the motions of thermal and electrical fluxes are directed in the same way. In contrast, for $\alpha < 0$, the thermal and electrical fluxes are directed in opposite directions; see Feldhoff and Geppert (2014b), Feldhoff (2015). By additively connecting several of these basic units thermally in parallel and electrically in series, the electric potential φ can be increased over the device to provide an important electric energy flux density at device output according to eq. [2]; see Feldhoff (2015) for illustration. The choice of the thermoelectric materials that comprise the TEG depends on the conditions in which the energy conversion is to be performed.

Among the various thermoelectric materials, semiconductors exhibit the best thermoelectric performance because of their moderate charge carrier concentration, and they provide a good balance between specific electrical conductivity σ and the Seebeck coefficient α; see Ioffe (1957). Consequently, semiconductors provide a high value of the so-called power factor $\sigma \cdot \alpha^2$, which is the charge-coupled entropy conductivity and occurs as part of the thermoelectric tensor in eq. [3]. To obtain a good TEG performance, the combination of n- and p-type semiconductors and a low-resistance electrical connection between them realized by metals or alloys is preferred. In commercially available generators, $Bi_{2-x}Sb_xTe_3$-based materials are primarily used; see Kuznetsov et al. (2002), Poudel et al. (2008). Additionally, the geometric properties of the materials that are combined to form the complete device have to be optimized for every system. Finite-element method (FEM) simulations are useful for calculating the thermoelectric performance in terms of the used materials and their geometric properties without constructing a real TEG. The thermoelectric properties can be measured over each individual material. Afterwards, the materials can be combined in a simulated TEG system with a specific geometry. Because the device does not have to be constructed, FEM simulations provide results ecologically, flexibly and rapidly. The objective of the present study is to demonstrate that FEM simulations are useful for predicting the thermoelectric properties of a TEG.

Experimental

Thermoelectric Measurement Setup

To estimate the thermoelectric characteristics of the TEG, it was placed between a heat source (heated copper plate) and a heat sink (water-cooled copper plate). The device was fixed with a clamping force of 0.6 kN, as indicated by a dynamometer. A schematic illustration of the measurement setup is shown in Figure 1. To provide good thermal surface contact, thermal grease with a specific thermal energy conductivity of $\lambda > 1.46 \mathrm{W(mK)}^{-1}$ in the temperature range of ca. 300–550 K was used as the interface material. The temperature was monitored using thermocouples. The voltage $U = \Delta\varphi$ was measured as the drop of the electric potential on the external load R_{load}. Due to the low internal resistance R_{module} of the thermoelectric generator (see Table 4), the electric current I was estimated indirectly:

$$I = \frac{U}{R_{\mathrm{load}}} \quad [4]$$

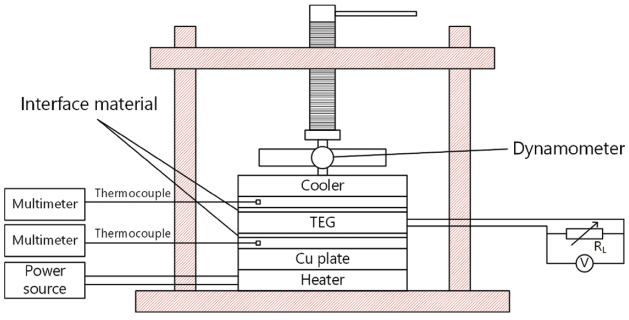

Figure 1: Schematic illustration of the measurement setup for determining the thermoelectric characteristics of the TEG with thermal grease as the interface material, after Hejtmanek et al. (2014).

The electric output power P_{el} was estimated according to:

$$P_{el} = \frac{U^2}{R_{\text{load}}} \quad [5]$$

Estimation of the Geometric and Thermoelectric Properties of the Thermoelectric Generator

A commercially available thermoelectric generator was purchased from Conrad Electronics SE (item number 193593–62, model number 1–7105). To construct the TEG in the model system, the geometry of the device, including the thermoelectric legs, the electric copper connectors and the alumina cover plates, were determined using the graphical tool ImageJ, which was applied to photomicrographs; see Schneider, Rasband, and Eliceiri (2012). Figure 2 presents photographs of the TEG and of the device modeled based on the estimated geometry for each individual component.

The TEG includes $12^2 - 2 = 142$ legs. The space between each pair of legs is 1 mm. Table 1 lists the geometric properties of the TEG without considering the tin solder. The geometric properties were estimated by analyzing the photographs shown in Figure 2. The relevant parameters are the length L of each material parallel to the entropy flux and its cross-sectional area A. The filling factor of the module, i.e., the ratio of thermoelectric active to inactive areas, is equal to 32%. For the copper connectors and alumina cover plates, the values for the specific resistivity ρ and specific thermal energy (heat) conductivity λ were taken from the literature; see Lide (2008). For the thermoelectric $Bi_{2-x}Sb_xTe_3$ materials, the specific thermal energy (heat) conductivity λ was also taken from the literature; see Kim et al. (2012). The

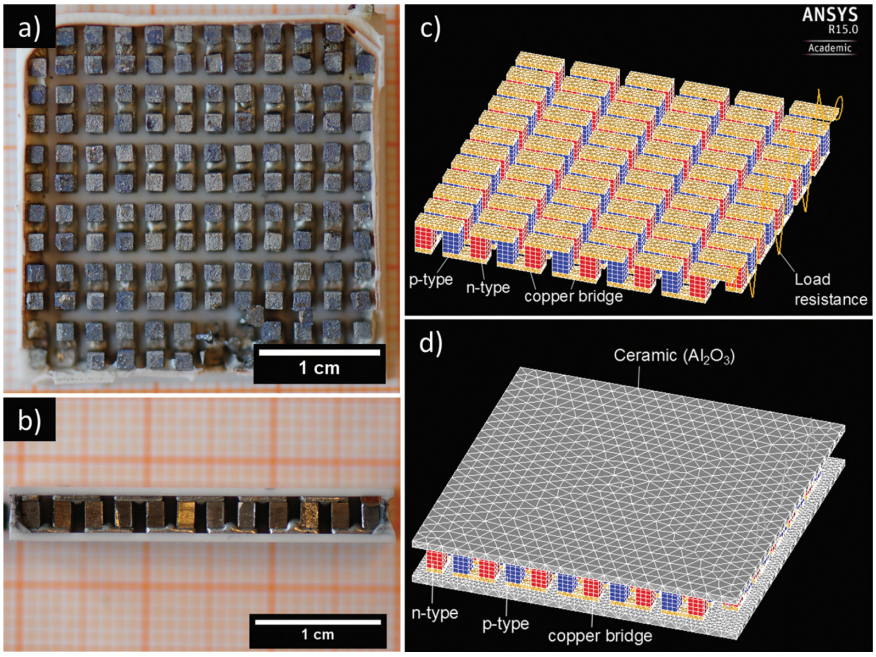

Figure 2: Photographs of the TEG for estimating the geometrical parameters and display of the modeled device; (a) inner top view of the TEG, (b) side view of the TEG, (c) modeled device with n- and p-type thermoelectric material and electric copper connectors, (d) modeled device with Al_2O_3 cover plates.

Table 1: Measured geometric properties of the TEG.

Component	Material	L/mm	A/mm^2	ρ/Ωm	λ/W(mK)$^{-1}$	Λ/Wm^{-1}K^{-2}
TE leg(n,p)	$Bi_{2-x}Sb_xTe_3$	2.05	1.96	see Table 4	1.05	$3{\cdot}10^{-3}$
Electric connector	Cu	0.44	5.32	$2.06{\cdot}10^{-8}$	401	1.15
Cover plates	Al_2O_3	0.64	870	$1{\cdot}10^{16}$	30.5	$8.71{\cdot}10^{-2}$

Notes: Length L of material and cross-sectional area A. The specific thermal energy resistivity ρ and specific thermal energy (heat) conductivity λ were taken from the literature as indicated in the text. The specific entropy conductivity λ was estimated according to eq. [6]. All data refer to a medial temperature of 350 K.

temperature-averaged values for the specific entropy conductivity Λ in Table 1 were calculated for a medial temperature of 350 K according to:

$$\lambda = T \cdot \Lambda \quad [6]$$

The specific electrical resistivity $\rho = \frac{1}{\sigma}$ of the thermoelectric material is the reciprocal of the specific electrical conductivity σ, and it was estimated under the temperature drops listed in Table 4. The systematic error, which results from the deviation from isothermal conditions (i.e. $\nabla T = 0$) according to requirements of eq. [3], however, is assumed to be small.

The Seebeck coefficient α was experimentally determined under electric open-circuited conditions (i.e. $\vec{j}_{q=0}$), for which eq. [3] provides:

$$\alpha = -\frac{\vec{\nabla}\varphi}{\vec{\nabla}T} \approx -\frac{\left(\frac{\Delta\varphi}{L}\right)}{\left(\frac{\Delta T}{L}\right)} = -\frac{\Delta\varphi}{\Delta T} \quad [7]$$

As expressed by eq. [7], for balanced gradients of potentials referring to a sample of length L, the gradients ∇ can be substituted by the drops Δ of potentials along this length.

Microstructure Analysis

A basic unit was cut from the thermoelectric generator and polished using diamond-lapping films (Allied High Tech Multiprep) for field-emission scanning electron microscopy (FE-SEM) investigations using a JEOL JSM-6700F, which was equipped with an Oxford Instruments INCA 300 energy-dispersive X-ray spectrometer (EDXS) for elemental analysis. The phase composition of the bulk n- and p-type $Bi_{2-x}Sb_xTe_3$-legs was analyzed by X-ray diffraction (XRD) using a Bruker D8 Advance with Cu-K_α radiation. The legs were isolated from the TEG and prepared for XRD measurements by pressing the ductile material onto the sample holder to increase the detectable area of the samples. This preparation approach caused an orientation in the crystal structure, which was considered in the analysis of the diffraction data. The XRD measurement results were analyzed using the Rietveld method as implemented in Topas 4.2. The reference data for the structure analysis were taken from the Inorganic Crystal Structure Database (ICSD).

Finite-Element Simulations

Using a script-based input process referring to the Analysis System (ANSYS), changes in thermoelectric properties as a result of changing material parameters, such as the composition and geometry of the considered materials, and the number of legs can be rematched very easily. The used ANSYS version is 15.0 academic. The script-based input tool uses the ANSYS Parametric Design Language (APDL). The simulation process can be separated into three basic steps: preprocessing, solving and postprocessing. During the preprocessing step, the geometric properties are created, the material's properties are set, the model is meshed and additional conditions are defined. Meshing determines the number of elements of the model and their nodes. The accuracy is given by the network's density. After the preprocessing is complete, solving of the grid points is executed. During the postprocessing step, the results are exported as plots, tables or figures. In this work, as mentioned in Section "Estimation of the Geometric and Thermoelectric Properties of the Thermoelectric Generator", a commercially available TEG was measured to estimate the average data for the thermoelectric properties and to evaluate a model system created using the FEM simulation tool. The modeled device consists of 72048 elements. Each thermoelectric leg is build up by 36 elements (total number of elements for the thermoelectric legs is 5,112) while each electric copper connector contains 220 elements (total number of elements for the electric copper connectors is 31,460). Each alumina cover plate consists of 17,138 (total number of elements for the alumina cover plates is 35,476). The non-linear solution converged after equilibrium iteration 2.

Results and Discussion

Microstructure of Materials

To estimate the elemental composition of the thermoelectric materials using the EDXS method in the FE-SEM, a two-leg fragment was cut from the TEG and polished. The SEM micrograph in Figure 3(a) shows the thermoelectric n- and p-type $Bi_{2-x}Sb_xTe_3$, the electric copper connectors and the alumina cover plates. The geometrical parameters are the same as those obtained from the photomicrograph of Figure 2(a), (b). Figure 3(b)–(f) shows the EDXS elemental distribution in the device by bright contrast.

Figure 4 presents the EDX spectra of the n- and p-type material (areas of analysis are marked in Figure 3(a)). The EDXS analysis does not detect any amount of antimony inside the n-type thermoelectric semiconductor. However, Kouhkarenko et al. (2001) reported that doping with a certain amount of antimony, approximately 25 at.% in the bismuth telluride structure,

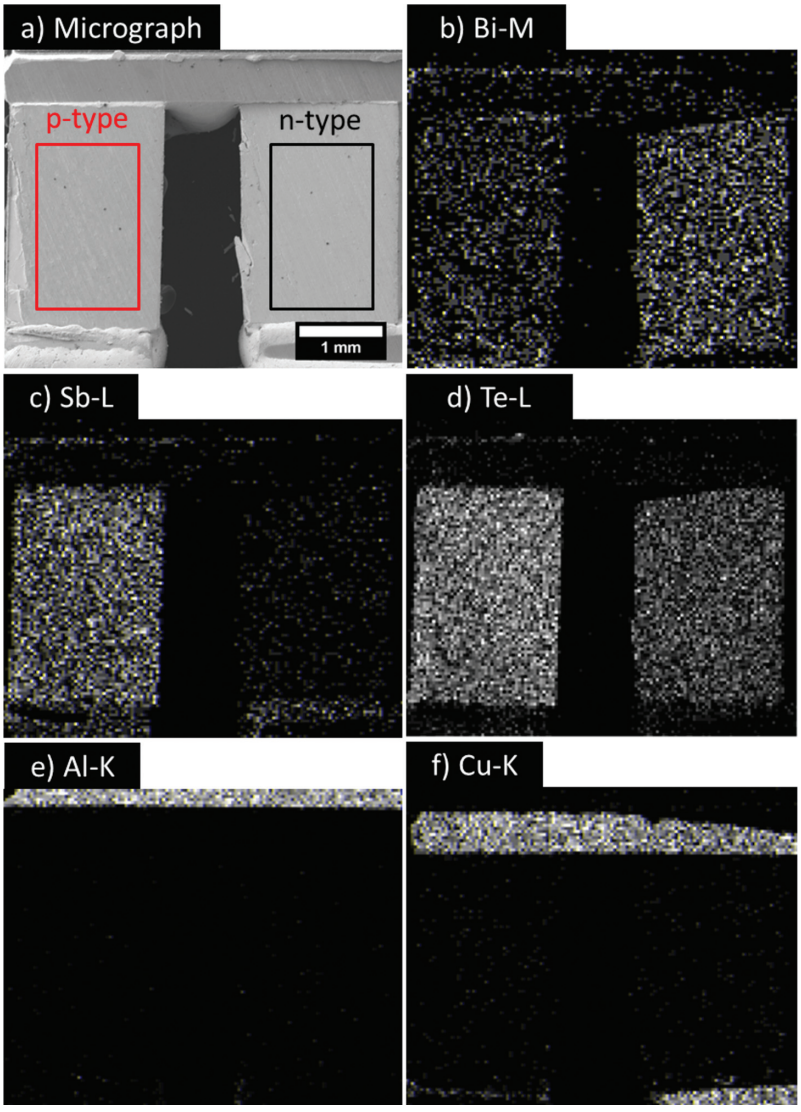

Figure 3: Side view of basic unit of the TEG exhibiting p- and n-type thermoelectric legs; (a) secondary electron micrograph, (b) Bi-M, (c) Sb-L, (d) Te-L, (e) Al-K, (f) Cu-K. Rectangularly marked areas in (a) refer to EDX spectra shown in Figure 4.

leads to an improvement in the Seebeck coefficient α of the n-type thermoelectric material. The thermoelectric properties of $Bi_{2-x}Sb_xTe_3$ are also influenced by the ratio of (Bi,Sb) and Te; see Fleurial et al. (1988). The ideal ratio for a stoichiometric composition $(Bi, Sb)_2Te_3$ is $\frac{(Bi,Sb)}{Te} = \frac{2}{3} = 0.667$. Within the accuracy of quantitative EDXS, both materials (n-type and p-type) match this value, which supports the assumption that the materials have been made according to the strategy described by Kouhkarenko et al. (2001).

The composition of the analyzed materials of the TEG is as expected. As indicated by the XRD pattern in Figure 5, the structure is preferentially orientated with the c-axis perpendicular to the sample holder, which is confirmed by the appearance of lattice reflections from the (0 0 l) planes with $l = 9$, 12, 15 (main reflection), 18, and 21. Furthermore, reflections from the (1 0 l) planes with $l = 10$, 13, 25, 28 are present, which, however, indicates only a slight tilt away from the c-axis. For refinement of the crystal structure, the preferred orientation resulting from the preparation (pressing of ductile material onto the sample holder) has to be considered. Because of the considerable amount of the Sb in the p-type material, the lattice parameters for this composition are smaller than those for the n-type material. The radii for structure-building elements can be extracted from Shannon (1976). With a medial coordination number of 6, it is 76 pm for Sb^{3+}, 103 pm for Bi^{3+}, and 221 pm for Te^{2-}. For the n-type material, which contains only Bi on the cationic site, the diffraction data were fitted to the

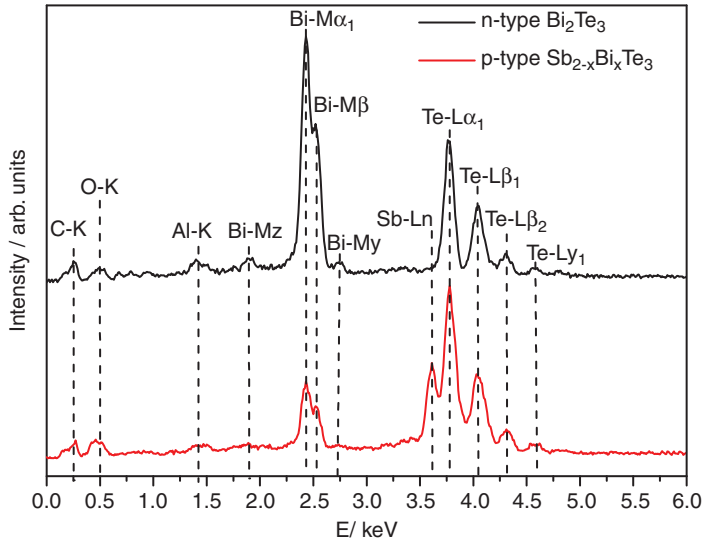

Figure 4: EDX spectra of n- and p-type thermoelectric legs according to the rectangular areas marked in Figure 3(a).

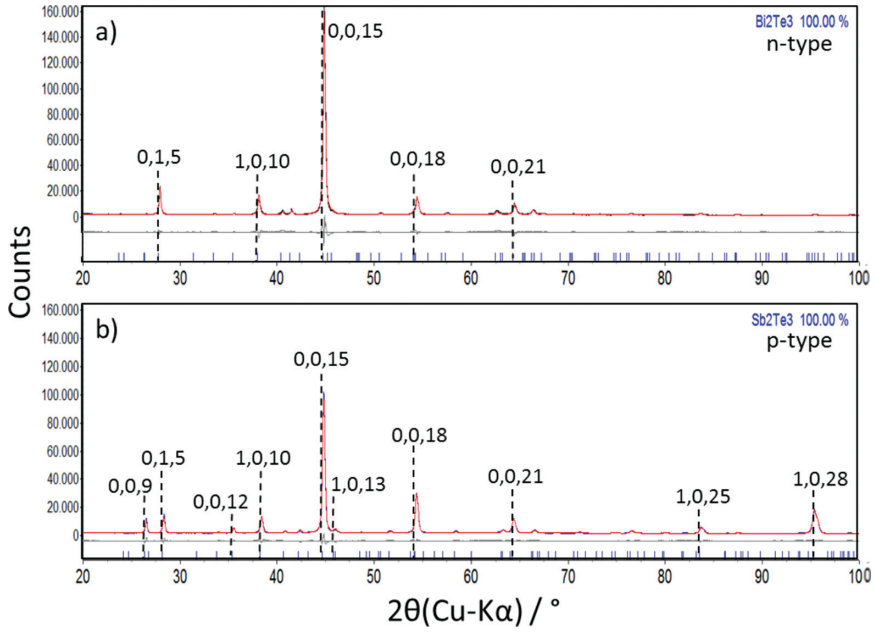

Figure 5: Scanned (black curve) and refined (red curve) X-ray diffraction data with difference curve (light gray); (a) n-type Bi_2Te_3, (b) p-type $Sb_{2-x}Bi_xTe_3$.

reference structure of Bi_2Te_3. For the p-type material, which contains a large amount of Sb on the cationic site, the diffraction data were fitted to the reference structure of Sb_2Te_3. The lattice parameters that were calculated by fitting the diffraction data to the aforementioned reference structures are listed in Table 2.

The results for the atomic positions considering the goodness of the Rietveld fit are listed in Table 3. The coordinates $x = 0$ and $y = 0$ are fixed. The goodness of fit (GOF) is expressed by the R-weighted pattern R_{wp} and R-expected R_{exp}. For the fit criteria used in Topas 4.2 see Young (1993).

Thermoelectric Investigations

To estimate the thermoelectric properties of the TEG, the measurement data were analyzed and the average values for the specific electrical conductivity σ (T), the Seebeck coefficient α (T) from the thermovoltage $U(T)$ and the

Table 2: Lattice parameters and unit cell volumes obtained from the Rietveld refinement and comparison to references. The space group, No. 166, is represented in hexagonal axes.

Stoichiometry	Description	Space group	a/Å	c/Å	V_{cell}/Å^3
Bi_2Te_{3-y}	Measured (n-type)	R-$\bar{3}$mH	4.367	30.401	502.01
Bi_2Te_3	ICSD: 158366	R-$\bar{3}$mH	4.385	30.497	502.82
$Sb_{2-x}Bi_xTe_{3-y}$	Measured (p-type)	R-$\bar{3}$mH	4.280	30.439	482.89
Sb_2Te_3	ICSD: 2084	R-$\bar{3}$mH	4.264	30.458	479.59

Table 3: Atomic positions and goodness of fit for the Rietveld refinement of the X-ray diffraction data presented in Figure 5. The coordinates $x = 0$ and $y = 0$ are fixed.

Description	Atom	Site	z coordinate ICSD	z coordinate Rietveld	R_{wp}	R_{exp}	GOF
n-type	Bi1	6 c	0.3985	0.3993	9.22	1.87	4.93
	Te1	3 a	0.0	0.0			
	Te2	6 c	0.7919	0.7906			
p-type	Sb1	6 c	0.3988	0.3986	8.54	1.88	4.53
	Te1	6 c	0.7872	0.7874			
	Te2	3 a	0.0	0.0			

temperature difference ΔT for the thermoelectric materials were calculated. The electronic and thermal quantities for copper and alumina were taken from Lide (2008) and are presented in Table 1. A summary of the electronic, thermal and thermoelectric parameters of the thermoelectric materials is given in Table 4. The specific resistivities ρ_{leg} of the legs were estimated from the absolute resistivity of the complete device R_{module} by considering the number of thermoelectric legs and their geometry. The Seebeck coefficient α_{leg} was estimated from the open-circuit voltage U_{OC} according to eq. [7]. Because the coefficient was averaged over all integrated legs, the same absolute values for n- and p-type legs are obtained, and the Seebeck coefficient becomes $\pm\alpha_{\mathrm{leg}}$. The maximum electric current I_{SC} under electric short-circuited conditions (i.e. $U = \Delta\varphi = 0$) and the maximum electric output power P_{max} are listed. All quantities are related to the established temperature drops ΔT and the medial temperature of the device T_{medial}.

To determine the thermoelectric parameters of the device, five temperature differences ΔT were established, which are indicated in Table 4 and Figures 6 and 7. Figure 6 shows U–I curves with good agreement between the FEM simulation (solid line) and measurement (data points) for all temperature conditions. Note, that the slope of the lines refers to the internal resistance R_{module}, as indicated in Table 4. The electric output power P_{el} was estimated in terms of different load resistivities R_{load}. Figure 7 shows good agreement between the experimental $P_{el} - I$ curve (data points) and the FEM simulation (solid line).

The results of the thermoelectric behavior can be shown in a vectorial plot that refers to the density of transported quantities, the thermal energy flux density $\vec{j}_{E,th}$ and the electric flux density $\vec{j}_q$. Figure 8 shows the results of the FEM simulation of the properties of the TEG's components at the maximum electric power output for a chosen temperature difference of 58 K. The colors of

Table 4: Determined thermoelectric parameters of the TEG (complete device) and single legs for different temperature conditions.

T_{hot}/K	ΔT/K	T_{medial}/K	R_{module}/Ω	ρ_{leg}/μΩ · m	α_{leg}/μV · K^{-1}	P_{max}/mW	U_{OC}/mV	I_{SC}/mA
373	58	344	2.28	15.35	± 142.18	144.59	1171	530.74
358	43	337	2.39	16.10	± 158.53	90.42	968	422.97
343	33	327	2.30	15.49	± 144.05	47.42	675	291.08
328	25	316	2.27	15.29	± 131.55	23.22	467	206.45
313	13	307	2.65	17.84	± 107.80	3.73	199	79.75

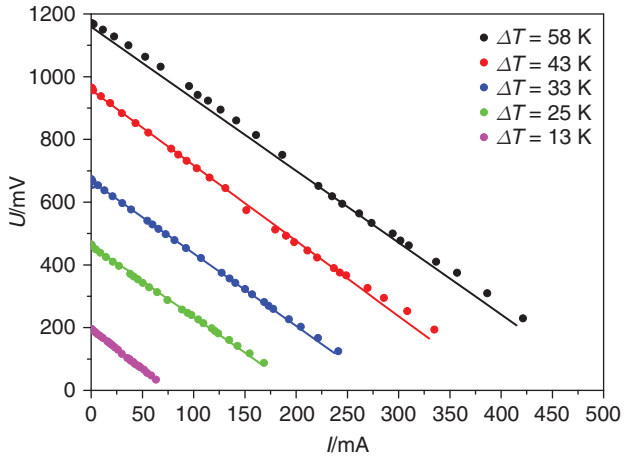

Figure 6: Comparison of measured (dots) and simulated (lines) decrease in voltage over electrical current in terms of load resistance R_L and temperature difference ΔT.

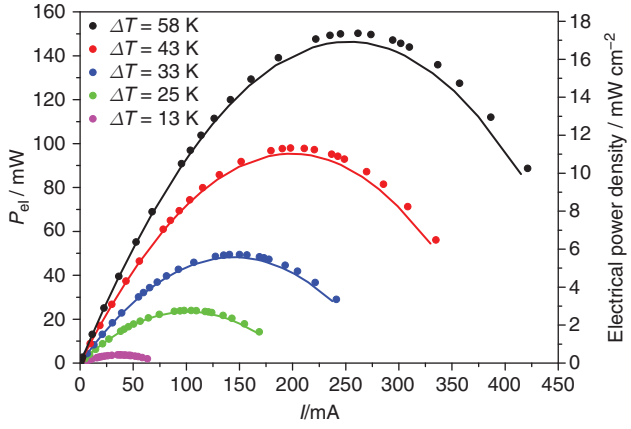

Figure 7: Comparison of measured (dots) power characteristics and simulated (lines) parameters in terms of load resistance R_L and temperature difference ΔT.

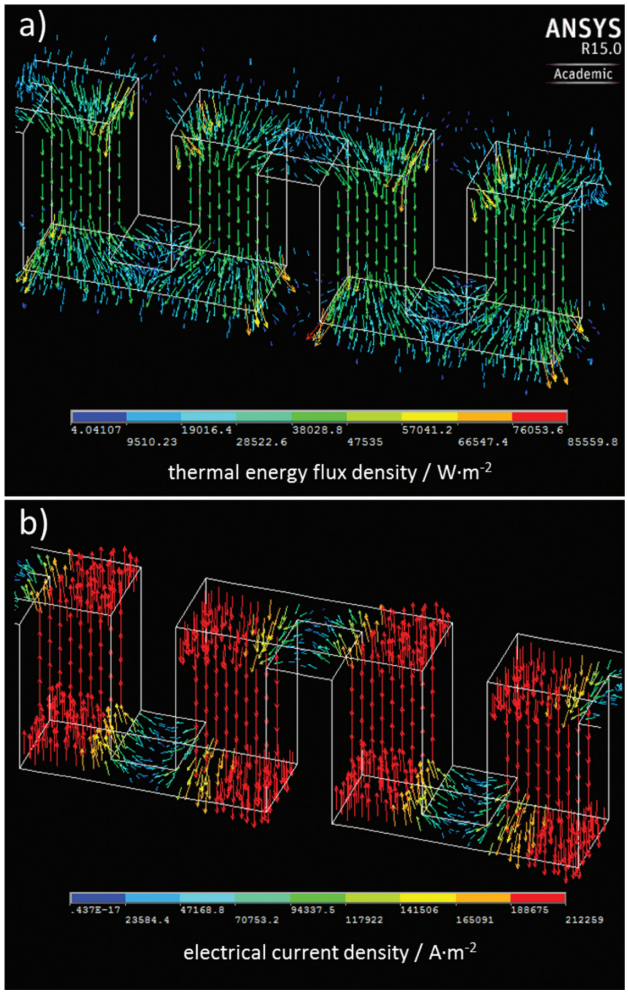

Figure 8: Flux densities of transported quantities with an established temperature difference of 58 K for conditions of maximum electric power output. (a) thermal energy flux density $\vec{j}_{E,th}$, (b) electric flux density $\vec{j}_q$.

the vectors refer to the local value of the density of the transported quantity, which is in indicated in the legend. The flux densities of thermal energy $\vec{j}_{E,th}$ and electric charge $\vec{j}_q$ depend on the material of the TEG's components and on the local potential gradients according to the potential distributions of Figure 9. The Al_2O_3 cover plates are not displayed but the flux densities at their location are. From Figure 8(a), it is clear that the thermal power density $\vec{j}_{E,th}$ is distinctly smaller in the region of the Al_2O_3 cover plates ($4\mathrm{W/m^2}$) than in the copper connectors ($2-4\cdot10^4\mathrm{W/m^2}$) or the thermoelectric $Bi_{2-x}Sb_xTe_3$ legs ($4-5\cdot10^4\mathrm{W/m^2}$). Due to the extremely high electric resistivity of the Al_2O_3 cover plates (see Table 1), the electric current density $\vec{j}_q$ vanishes at their location. In the copper connectors, it amounts to $\vec{j}_q = 1\cdot10^{-17} - 2\cdot10^5\mathrm{A/m^2}$ with strong local variation, and it is highest in the thermoelectric legs ($2\cdot10^5\mathrm{A/m^2}$). Note that fluxes of thermal energy and electric charge are co-aligned in the case of p-type legs and counter-aligned in the case of n-type legs.

Figure 9(a) shows the distribution of the entropy potential T, obtained from the FEM simulation and a cross-section of the TEG at maximum electric power output for a potential drop of $\Delta T = 58\,\mathrm{K}$. Figure 9(b) shows the respective distribution of the electric potential $U = \Delta\varphi$ along the electric serial connection of the assembled thermoelectric legs and copper connectors inside the module. When the potential at the electric input is at ground (i.e. $\varphi = 0$), it continuously increases along the chain to be $\varphi = 571\,\mathrm{mV}$ at the electric output. Note that this value is identical to the voltage at the electric power maximum (from Figure 7) in Figure 6 for the same temperature drop. The modeling of TEGs using

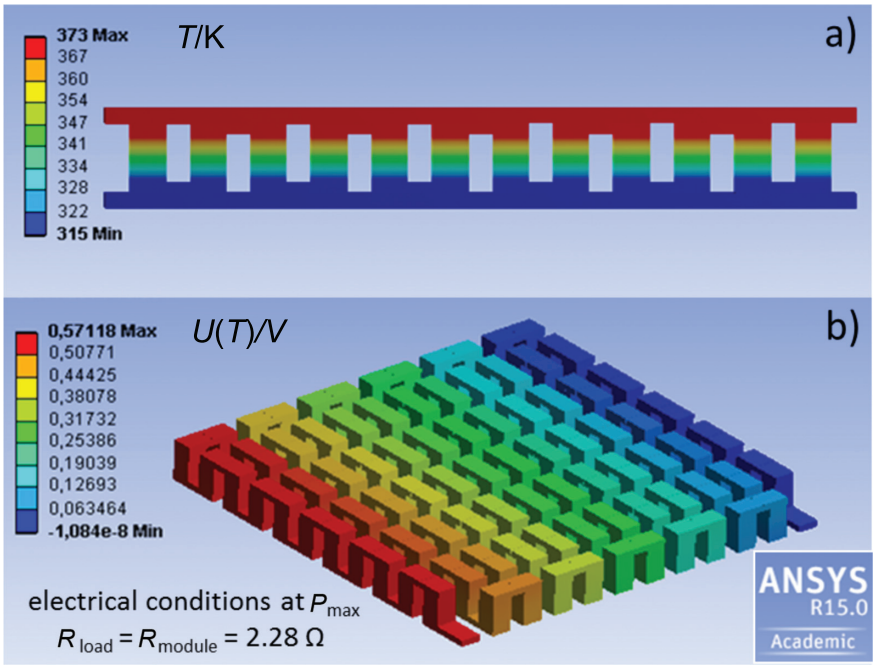

Figure 9: Potential distributions in the TEG at the electric power maximum and referring to the temperature difference of 58 K as obtained from the finite-element simulation: (a) temperature distribution referring to the local entropy potential, (b) established electric potential.

the FEM method has the advantage of providing deep insight into the distribution of all relevant quantities throughout the entire module.

The results from the finite-element simulation illustrate the relation between the entropy potential T and electric potential φ, which is given algebraically in eq. [3] by the respective gradients, and the obtained flux densities $\vec{j}_{E,th}$ (see eq. [1]) and $\vec{j}_q$.

Conclusions

The model thermoelectric system created from the finite-element simulation provides results with acceptable accuracy. The latter is estimated from the good agreement between simulation and experimental data in the case of voltage–electric current ($U - I$) curves and electric power–electric current ($P_{el} - I$) curves for different temperature situations. Deep insights into the local variations of the relevant thermoelectric parameters can be obtained from this type of modeling. Overall, the developed model system can predict the thermoelectric properties of a certain TEG quite well if the proper parameters for feeding the simulation tool are selected. Work on thermoelectric materials and systems benefits from the use of FEM simulations to check the properties before constructing a device. The properties of the regarded systems can be varied very easily, thus making FEM tools a very flexible possibility for predicting the power characteristics of a thermoelectric device in terms of the requirements for its application.

References

Falk, G., F. Herrmann, and G. Schmid. 1983. "Energy Forms or Energy Carriers?" *American Journal of Physics* 51: 1074–77.

Feldhoff, A. 2015. "Thermoelectric material tensor derived from the Onsager – de Groot – Callen model." *Energy Harvesting and Systems* 2 (1): 5–13.

Feldhoff, A., and B. Geppert. 2014a. "Erratum to EHS 1 (1–2), 69–78 (2014): A High-Temperature Thermoelectric Generator Based on Oxides." *Energy Harvesting and Systems* 1 (3–4): 251.

Feldhoff, A., and B. Geppert. 2014b. "A High-Temperature Thermoelectric Generator Based on Oxides." *Energy Harvesting and Systems* 1 (1–2): 69–78.

Fleurial, J., L. Gailliard, R. Triboulet, H. Scherrer, and S. Scherrer. 1988. "Thermal Properties of High Quality Single Crystals of Bismuth Telluride – Part I: Experimental Characterization." *Journal of Physics and Chemistry of Solids* 49: 1237–47.

Fuchs, H. 2010. *The Dynamics of Heat – A Unified Aproach to Thermodynamics and Heat Transfer*. 2nd edition. Graduate Texts in Physics. New York, NY: Springer.

Fuchs, H. 2014. "A Direct Entropic Approach to Uniform and Spatially Continuous Dynamical Models of Thermoelectric Devices." *Energy Harvesting and Systems* 2: 1–13.

Hejtmanek, J., K. Knizek, V. Svejda, P. Horna, and M. Sikora. 2014. "Test System for Thermoelectric Modules and Materials." *Journal of Electronic Materials* 43: 3726–32.

Ioffe, A. 1957. *Semiconductor Thermoelements and Thermoelectric Cooling*. 1st edition. London: Infosearch Ltd.

Kim, C., D. H. Kim, H. Kim, and J. S. Chung. 2012. "Significant Enhancement in the Thermoelectric Performance of Bismuth Telluride Nanocompound Through Brief Fabrication Procedures." *ASC Applied Materials and Interfaces* 4: 2949–54.

Kouhkarenko, E., N. Frety, V. G. Shepelevich, and J. C. Tedenac. 2001. "Electrical Properties of $Bi_{2-x}Sb_xTe_3$ Materials Obtained by Ultrarapid Quenching." *Journal of Alloys and Compounds* 327: 1–4.

Kuznetsov, V. L., L. A. Kuznetsova, A. E. Kaliazin, and D. M. Rowe. 2002. "High Performance Functionally Graded and Segmented Bi_2Te_3-Based Materials for Thermoelectric Power Generation." *Journal of Materials Science* 37: 2893–97.

Lide, D. 2008. *CRC Handbook of Chemistry and Physics*. 89th edition. Internet Version 2009. Boca Raton, FL: CRC Press.

Poudel, B., Q. Hao, Y. Ma, Y. Lan, A. Minnich, B. Yu, X. Yan, D. Wang, A. Muto, D. Vashaee, et al. 2008. "High-Thermoelectric Performance of Nanostructured Bismuth Antimony Telluride Bulk Alloys." *Science* 320: 634–38.

Schneider, C., A. Rasband, and K. Eliceiri. 2012. "NIH to ImageJ: 25 Years of Image Analysis." *Nature Methods* 9: 671–75.

Shannon, R. 1976. "Revised Effective Ionic Radii and Systematic Studies of Interatomic Distances in Halides and Chalcogenides." *Acta Crystallographica* A 32: 751–67.

Young, R. 1993. *Introduction to the Rietveld Method*. IUCr Book series. Oxford: Oxford University Press.